13th International Symposium on Turbulence and Shear Flow Phenomena (TSFP13)
Montreal, Canada, June 25–28, 2024

DIRECT NUMERICAL SIMULATION OF INSTALLATION EFFECTS ON AIRFOIL NOISE

Ziyang Zhou
Mechanical Engineering Department
Université de Sherbrooke
Sherbrooke, Quebéc, J1K2R1, Canada
zhou.ziyang@usherbrooke.ca

Stéphane Moreau
Mechanical Engineering Department
Université de Sherbrooke
Sherbrooke, Quebéc, J1K2R1, Canada
stephane.moreau@usherbrooke.ca

Marlène Sanjosé
Mechanical Engineering Department
École de technologie supérieure
Montréal, QC, H3C 1K3 Canada
marlene.sanjose@etsmtl.ca

ABSTRACT

To evaluate installation effects on velocity statistics and its influence on farfield noise, three Direct Numerical Simulations (DNS) have been run using the Lattice-Boltzmann Method (LBM) with the PowerFLOW software on the Controlled-Diffusion (CD) airfoil at $Re = 150000$ and $\alpha = 8^\circ$ installed in the Universite de Sherbrooke (UdeS) wind tunnel. Differences in setup between these DNS simulations are the addition of voxel refinements and turbulent trips to the simulation setup for better capturing the shear layer downstream of the wind tunnel nozzle lip. Results show that the boundary layer displacement thickness, momentum thickness and shape factor are slightly increased after shear layer refinement due to an increase in mean angle of attack ($\overline{\alpha}$) caused by a change in shear layer state. Despite these changes caused by the mixing layer state, relevant wall-pressure, velocity statistics and far-field acoustic pressure are not significantly modified.

Introduction

Recent improvements in turbomachinery noise have led to a strong reduction of tonal noise in rotating machines. Broadband noise contribution is then becoming more and more important. When under clean and controlled inlet flow conditions, the main broadband noise source is the sound produced at the trailing edge of blades. Any turbulence or flow disturbance born in the boundary layer of any lifting surface generates pressure fluctuations and vorticity distortions that diffract at the trailing edge and produce acoustic waves.

Many numerical studies have tried to analyse the flow around airfoils to isolate the trailing-edge (TE) noise mechanisms because it is a canonical flow problem to investigate TE noise in turbomachines. In the present study, the flow around a controlled diffusion (CD) airfoil in an anechoic open-jet facility is investigated. The chord based Reynolds number is 1.5×10^5 and the Mach number is 0.05, characteristic of low speed fan systems. This configuration has become a reference case study for trailing-edge noise as both aerodynamic and acoustic data have been collected experimentally and numerically. The experimental database provides hotwire measurements to characterise the incoming flow, the boundary-layer on the suction side, near and far wake and the jet shear layers (Moreau *et al.*, 2006). Mean-pressure coefficient and wall-pressure spectra at several locations on the airfoil pressure and suction sides have also been measured (Roger & Moreau, 2004; Moreau & Roger, 2005). Far field sound and directivity spectra have been recorded in the mid-span plane of the mock-up.

The numerical database provides the results from various solvers of several Reynolds-Averaged Navier-Stokes (RANS) turbulent models applied on the wind tunnel configuration and compressible DNS simulations computed on restricted domains embedded in the potential core of the open jet (Wu *et al.* (2020); Arroyo *et al.* (2022)). Far-field noise has been predicted by applying the FWH analogy on the solid surface of the airfoil and on a porous surface enclosing the airfoil. Notably, discrepancies still exist between the two predictions and with experimental results at high frequencies. Furthermore, the validity of approximating the effect of the open jet using a mean flow field has yet to be determined. While previous works using the LBM (Sanjose *et al.*, 2014; Moreau *et al.*, 2019; Zhou *et al.*, 2023) have shown that the pressure distribution on the CD airfoil is sensitive to the state of the shear layer in the simulation, its effect on turbulent statistics has not yet been fully examined. According to Caiazzo *et al.* (2023), displacement thickness, edge velocity and Reynolds stress can serve as indicators of wall-pressure fluctuation intensity on the wall as they provide useful scaling parameters. Understanding the influence of installation effects on these parameters can shed light on the mechanism by which the installation influences far field acoustic pressure and guide future efforts to quantify its influence.

1 Numerical configuration

1.1 Computational Domain

The computational domain in this simulation, shown in Fig. 1, mimics several open-jet experimental set-ups (Moreau & Roger, 2005; Jaiswal *et al.*, 2020) including that in the ane-

choic wind tunnel facility at Université de Sherbrooke (UdeS) Jaiswal *et al.* (2023). The geometry of the open jet nozzle is included in the computational domain in a simplified manner. This is because accounting for the resultant installation effects are absolutely necessary to reproduce the proper loading on the airfoil and thus the proper turbulent boundary layer development on the suction side and consequently the noise radiated in the far field (Moreau *et al.*, 2003). The CD airfoil, placed in the potential core of this jet, has a chord length of $c = 0.1356$ m. The simulation is limited to a span width of $0.1\,c$ with periodic boundary conditions used in the spanwise direction. This span length has been demonstrated to be sufficient through previous studies by Wu *et al.* (2020) and Wang *et al.* (2009). The inlet velocity is 16 m/s with a coflow of 0.165 m/s. Boundary conditions are set as shown in Fig. 1. Pressure probes are set on the surface of the airfoil at locations corresponding to the Remote Microphone Probe (RMP) positions in experiments (Moreau & Roger, 2005; Jaiswal *et al.*, 2020) as shown in Fig. 2.

1.2 Numerical method

In the present study, the Lattice Boltzmann Method (LBM) (He & Luo, 1997; Chen, 1998) is used. The solver used is PowerFlow 6.2021.R6 and this solver is naturally transient and compressible leading to an insight on hydrodynamics mechanisms responsible for trailing edge (TE) noise sources. In LBM, the Boltzmann equation is solved on a lattice in order to obtain the discrete-velocity distribution function in the multi-dimension phase space, $f_i(\mathbf{x},t)$, where $\mathbf{x}$ is the particle position, $\mathbf{c}$ is the particle velocity and t is time. For the low speed conditions examined in this study, the classical D3Q19 lattice is used, which means that the three dimensional isothermal flow field is solved using 19 directions in-phase space. The classical BGK relaxation model is used for the collision operator. To obtain density ρ and momentum ρu, weighted sums of f_i are calculated (Krüger *et al.*, 2017):

$$\rho(\mathbf{x},t) = \sum_i f_i(\mathbf{x},t) \tag{1}$$

$$\rho\mathbf{u}(\mathbf{x},t) = \sum_i c_i f_i(\mathbf{x},t) \tag{2}$$

1.3 Mesh criteria

The discrete-velocity distribution function is defined in a lattice made up of cubic cells called voxels. The computational domain is then filled with a octree-grid of these voxels with a 1:2 grid refinement. In order to resolve smaller flow structures, voxel regions (VR) are defined in which the voxel size Δx is specified. 10 voxel regions, shown by the black lines in Fig. 1, are used in the computational domain. The voxel regions are used to impose the required y^+ on the surface of the airfoil and transition into larger cell sizes in areas further away. As shown in Fig. 4, $y^+ < 1.1$ is achieved on the airfoil surface.

Note also that although the experimental Mach number is 0.05, the Mach number has been increased in the simulation to 0.2. This adjustment is necessary to achieve DNS resolution in the three VR regions closest to the airfoil. To accommodate this Mach number increase, the lattice velocity must be raised, and consequently, lattice viscosity is also increased to maintain a constant Reynolds number. Due to a stability threshold on the relaxation time, the viscosity in VR regions beyond the three finest ones is higher than the specified kinematic viscosity of $1.44 \times 10^{-5}\,\frac{m^2}{s}$. As mentioned in Sanjose & Moreau (2011), the three finest VR regions cover the size of the boundary layer as measured by Neal (2010) in the MSU wind tunnel.

Compared to the original setup in Sanjose & Moreau (2011), additional voxel refinement regions have been used to capture the development of the turbulent boundary layer downstream of the zigzag trip inside the nozzle as shown in Fig. 3 resulting in a more turbulent jet shear layer. Details of the zigzag trip used and the voxel regions in the jet shear layer are given in Zhou *et al.* (2023). Using the LBM solver, the simulations shown in table 1 have been run for 30 through-flow times from which statistics are taken from the final 20 through-flow times. Note that the number of through flow times is significantly increased from the previous studies Wang *et al.* (2009); Christophe *et al.* (2009); Sanjose & Moreau (2011), which only used 5-6 through flow times to establish the turbulent flow statistics around the airfoil. This is in order to resolve the low frequency shear layer movements. In total, each case took 90 hours on 1440 Intel "Skylake" cores at 2.4 GHz.

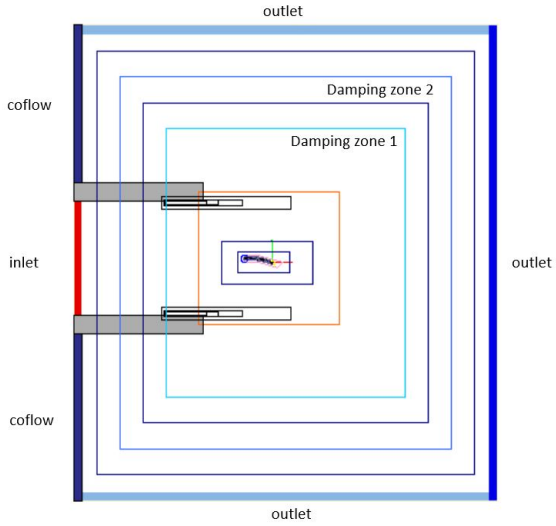

Figure 1. VR regions used for shear layer refinement.

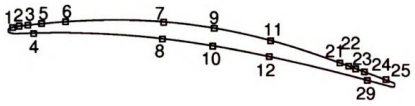

Figure 2. RMP location in the streamwise direction.

2 Results

This section will begin by highlighting the differences in flow features found in the 3 cases, followed by an analysis of the mean velocity and pressure profiles. Wall pressure statistics and far field noise will then ensue.

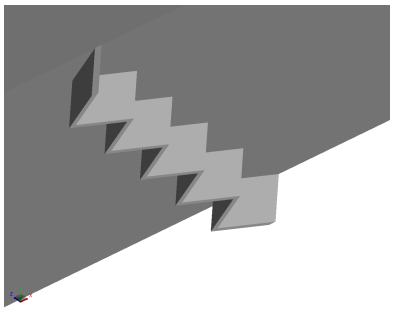

(a) Zigzag trip on Upper Lip

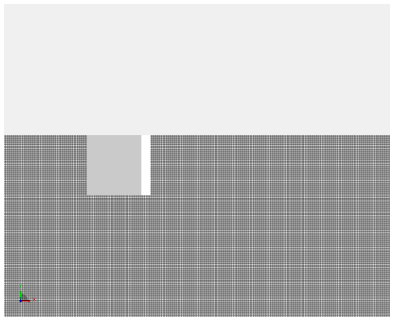

(b) Voxel Refinement for Turbulent Trip

Figure 3. Geometry and Mesh of Zigzag Trip.

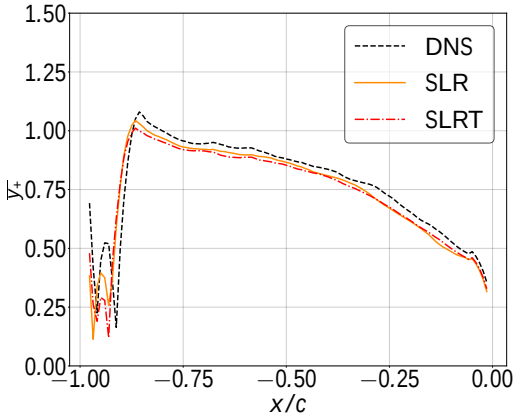

Figure 4. y^+ on the surface of the airfoil.

Table 1. CD Airfoil Studies

Name	Lip BC	Inlet BC	Trip	SLR
SLR	Slip	Profile	No	Yes
SLRT	No Slip	Uniform	Yes	Yes
DNS	Slip	Profile	No	No
Experiment	N/A	N/A	N/A	N/A

2.1 Flow Topology

Comparing DNS with DNS-SLR results in Fig. 5 reveals significant differences in the topology of the shear layer upstream of the airfoil due to refinement of the shear layers. In the original DNS case, the jet shear layer remained laminar up to the mid chord of the CD airfoil before transitioning to turbulence via Kelvin-Helmholtz instabilities. Conversely, with voxel refinement, the formation of Kelvin-Helmholtz instabilities occurred at the nozzle lip, leading to vortex pairing above the leading edge of the airfoil in the DNS-SLR case. The introduction of the zigzag trip led to boundary layer transition to turbulence upstream of the nozzle lip, mitigating the large instabilities involved in vortex pairing observed in the DNS-SLR case above the leading edge of the airfoil. As a result, vortex pairing occurred further downstream with the addition of the trip.

Due to differences in the development of the jet shear layer the instantaneous flow angle, or angle of attack correction ($\alpha_i = \tan^{-1}(U_y/U_x)$) measured 1 chord length upstream of the leading edge (LE), behaves differently in the 3 cases. While α_i is between 0.5 and 1 degrees for 20 through flow times as simulated in the DNS case, in the DNS-SLR and the DNS-SLRT cases the α_i is between 0.0 and 1.5. Note also that the mean angle-of-attack correction, $\overline{\alpha_i}$, is higher in the SLR and SLRT cases than in the DNS case.

2.2 Mean Pressure Coefficient

The mean aerodynamic loading on the airfoil may be observed using the mean pressure coefficient given by

$$\overline{C_p} = \frac{\overline{p} - p_{ref}}{\frac{1}{2}\rho_{ref}U_{ref}^2} \tag{3}$$

where p_{ref}, ρ_{ref} and U_{ref} are the reference pressure, density and velocity respectively, taken at the exit of the nozzle. In Fig. 7, good agreement between all numerical and experimental results is seen except in the LSB region at $-1.0 < x/c < -0.8$. In particular, the DNS-SLR and DNS-SLRT cases have smaller LSBs than the DNS case. This may be explained not only by the increase in turbulence intensity from 0.3% to 0.5% as mentioned in Zhou *et al.* (2023), but also by the change in geometrical angle of attack, α_i in Fig. 6.

2.3 Mean boundary-layer velocity profiles

The boundary layer profiles at 6 locations from the leading edge (LE) to the TE are shown in Fig 8. Near the LE, the DNS case contains a LSB that extends up to probe 5 while the transition to turbulence has already occurred at this location in the DNS-SLR and DNS-SLRT cases. In the zero pressure gradient (ZPG) region at probes 7 and 9, the 3 cases have similar thicknesses at mid-chord but the thickness deviates at the trailing edge at probes 21 and 24. As a result, as shown in Fig. 9(a), the DNS-SLR and DNS-SLRT cases show larger δ^* and δ_{95} than the DNS case at the TE. This is most likely caused by the discrepancy in $\overline{\alpha_i}$ which increased the adverse pressure gradient (APG) effects in both these cases. Despite this change, the 3 cases show similar shape factors to within 3 percent as seen in Fig. 9(b).

2.4 Reynolds stress

The normalized Reynolds stress, $uv^+ = \overline{uv}/u_\tau^2$, is also a relevant parameter for scaling of wall-pressure statistics as demonstrated by Caiazzo *et al.* (2023). Only the results for DNS and DNS-SLRT are plotted in Fig. 10 as only in these 2 cases were the velocity components at the required locations recorded for 20 through-flow times. At probe 7 in the zero pressure gradient (ZPG) uv^+ matches well with flat plate DNS results by Spalart (1988). As the trailing edge is approached, the profile deviates from flat plate results due to the influence

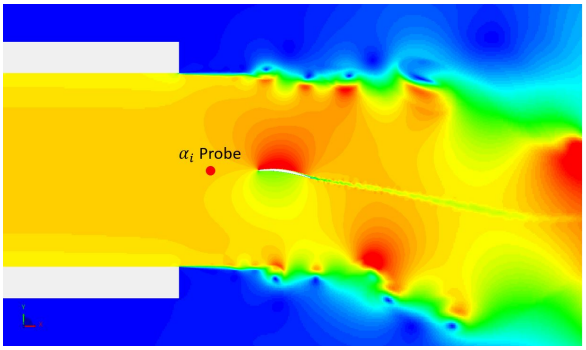

(a) DNS

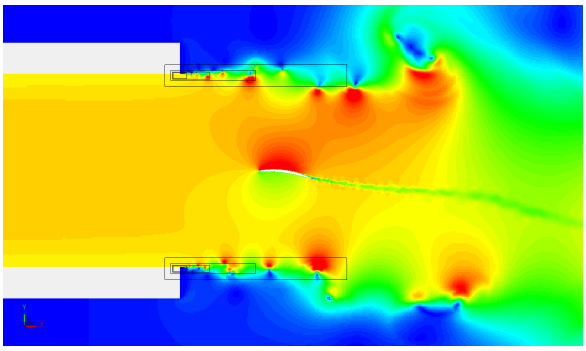

(b) SLR

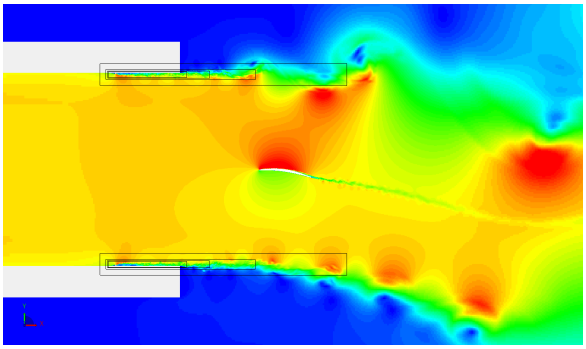

(c) SLRT

Figure 5. Mid plane velocity magnitude contours.

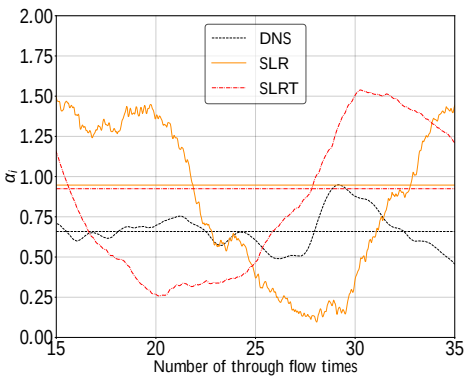

Figure 6. Correction of angle of attack (α_i). Horizontal straight lines show mean correction of angle of attack ($\overline{\alpha_i}$).

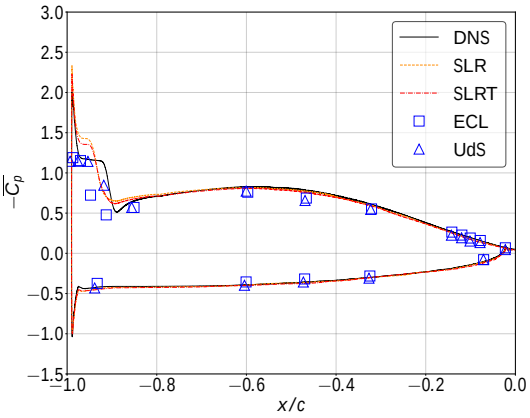

Figure 7. Mean pressure coefficient.

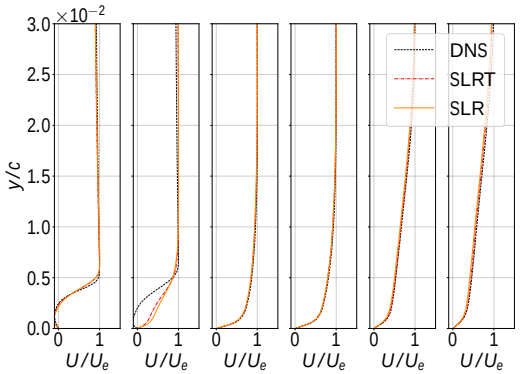

Figure 8. Boundary layer velocity profile at probes 3, 5, 7, 9, 21 and 24 (from left to right)

of the adverse pressure gradient as mentioned by Caiazzo *et al.* (2023). The SLRT profile shows a profile that is further offset from the wall, which is expected as the effect of having a higher δ_{95}. Despite this, the peak uv^+ is similar for both results which is indication that p_{rms} are of similar levels.

2.5 Velocity spectra

Before analysing the wall-pressure statistics, it is worth analysing the velocity spectrum to reveal if DNS resolution has been actually achieved in the boundary layer. This is done by plotting the one-dimensional streamwise velocity spectrum E_{11} in the DNS case. The Kolmogorov scale represents the smallest length scale of eddies in turbulent flow and is defined by $\eta = (\upsilon^3/\varepsilon)^{1/4}$ where $\varepsilon = 2\nu\overline{S_{ij}S_{ij}}$ is the dissipation rate and the strain rate is given by $S_{ij} = \frac{1}{2}(\frac{du_i}{dx_j} + \frac{du_j}{dx_i})$. Fig. 11 shows the normalized E_{11} at 4 locations in the boundary layer above probe 7 and probe 24 at $y^+ = 23$ and $y^+ = 69$ (see Fig. 2 for locations). As shown by the dotted lines in both figures, DNS resolution has been achieved at both locations. Similar results are expected for the DNS-SLR and DNS-SLRT cases.

2.6 Wall-pressure spectra

The power spectral density (PSD) of the 3 cases at probe 3 to probe 24 on the suction side of the airfoil are shown in Fig 12 for the 3 cases. The experimental results captured at UdeS and ECL are also included. At probe 3, the DNS case

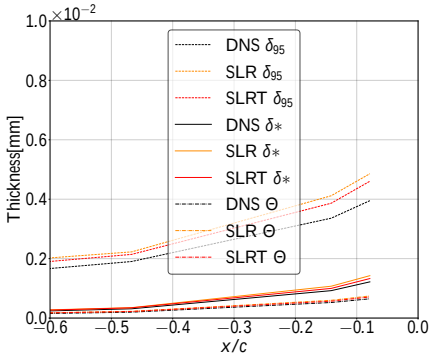

(a) Boundary layer thickness

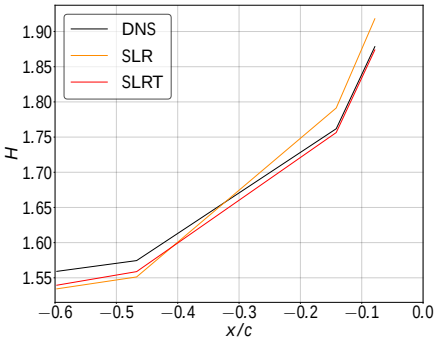

(b) Shape factor

Figure 9. Boundary layer parameters at attached flow locations.

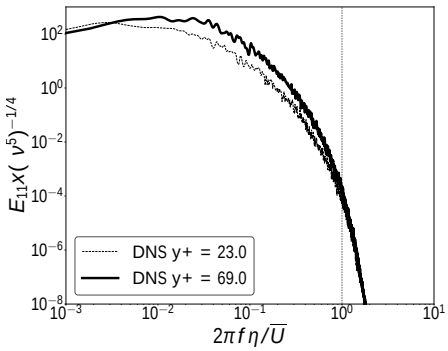

(a) Probe 7

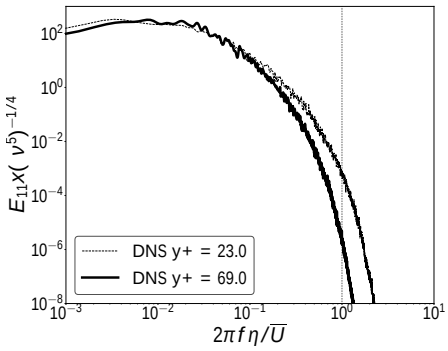

(b) Probe 24

Figure 11. Normalized streamwise velocity spectra.

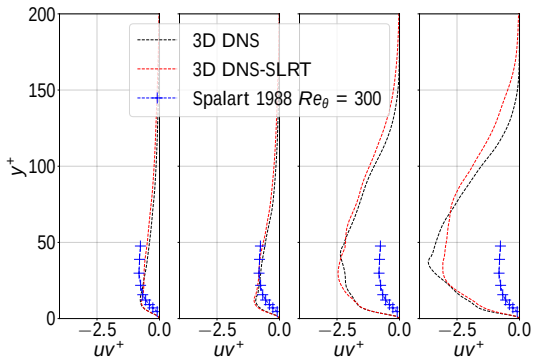

Figure 10. uv^+ at probes 7 (leftmost), 9, 21 and 24 (rightmost).

show lower spectral levels than the DNS-SLR and DNS-SLRT cases due to the probe being inside the LSB whereas the LSB begins to reattach at this location in the DNS-SLR and DNS-SLRT cases. At probe 5, an increase in spectral levels and a weaker broadband hump are seen for all the numerical cases. Downstream of the LSB reattachment (probe7 to probe 24), there is an overall good agreement between numerical simulation and the UdeS experimental results. The wall PSD levels between the 3 DNS cases are also similar.

2.7 Farfield noise

PSD of the far-field acoustic pressure are obtained using the Ffowcs-William and Hawking (FWH) analogy applied to the airfoil surface are compared with the measurements achieved at UdeS and ECL. The latter was taken at 2 m from the airfoil trailing edge and at 90° above the suction side and is represented by the black line in Fig. 13. As detailed in Zhou *et al.* (2023), the jet shear layer in the DNS-SLR case results in low frequency pressure footprints on the airfoil. In the mid range (1000 Hz to 5000 Hz), good agreement exists between all the DNS results as all three cases show the presence of a high frequency hump at 5000 Hz. This latter was shown by Zhou *et al.* (2023) to be coming from the LSB reattachment near the LE. It is not present in the DNS case because there is less LSB activity lower fluctuation in α_i. The corresponding plateau was also shown to be caused by an additional noise source in the wake (Wu *et al.*, 2020; Arroyo *et al.*, 2022).

3 Conclusion

Several DNS of the flow over a controlled-diffusion airfoil at a chord-based Reynolds number of 1.5×10^5, a Mach number of 0.2 and a 8° geometrical angle-of-attack, installed in a typical open-jet wind tunnel set-up have been achieved using LBM, to assess the effect of the jet state on the airfoil aerodynamics and emitted noise for the first time. Additional APG effects cased by a slight increase in $\overline{\alpha_i}$ in the DNS-SLR and DNS-SLRT cases caused a thicker LSB at the LE and the boundary layer to thicken at the TE. A slight offset away from the wall is also seen for uv^+ in the DNS-SLRT case but peak uv^+ remains at similar levels even at the TE. As a result , wall PSD downstream of the mid chord were similar for all cases, showing that differences in boundary layer statistics was not a main driver of far-field noise differences at this operating condition.